

PHOTONICS Research

All-optical nanoscale thermometry with silicon carbide color centers

CHENGYING LIU,^{1,†} HAIBO HU,^{1,2,†} ZHENGTONG LIU,² SHUMIN XIAO,^{1,2} JUNFENG WANG,^{5,6} YU ZHOU,^{1,3,*} AND QINGHAI SONG^{1,3,4,7} 

¹Ministry of Industry and Information Technology Key Laboratory of Micro-Nano Optoelectronic Information System, Guangdong Provincial Key Laboratory of Semiconductor Optoelectronic Materials and Intelligent Photonic Systems, Harbin Institute of Technology, Shenzhen 518055, China

²Pengcheng Laboratory, Shenzhen 518055, China

³Quantum Science Center of Guangdong-Hong Kong-Macao Greater Bay Area, Shenzhen-Hong Kong International Science and Technology Park, Shenzhen 518045, China

⁴Collaborative Innovation Center of Extreme Optics, Shanxi University, Taiyuan 030006, China

⁵College of Physics, Sichuan University, Chengdu 610065, China

⁶e-mail: jfwang@scu.edu.cn

⁷e-mail: qinghai.song@hit.edu.cn

[†]The authors contributed equally to this work.

*Corresponding author: zhouyu2022@hit.edu.cn

Received 11 April 2024; revised 10 June 2024; accepted 15 June 2024; posted 18 June 2024 (Doc. ID 525971); published 1 August 2024

All-optical thermometry plays a crucial role in precision temperature measurement across diverse fields. Quantum defects in solids are one of the most promising sensors due to their excellent sensitivity, stability, and biocompatibility. Yet, it faces limitations, such as the microwave heating effect and the complexity of spectral analysis. Addressing these challenges, we introduce a novel approach to nanoscale optical thermometry using quantum defects in silicon carbide (SiC), a material compatible with complementary metal-oxide-semiconductor (CMOS) processes. This method leverages the intensity ratio between anti-Stokes and Stokes emissions from SiC color centers, overcoming the drawbacks of traditional techniques such as optically detected magnetic resonance (ODMR) and zero-phonon line (ZPL) analysis. Our technique provides a real-time, highly sensitive (1.06 K^{-1}), and diffraction-limited temperature sensing protocol, which potentially helps enhance thermal management in the future miniaturization of electronic components. © 2024 Chinese Laser Press

<https://doi.org/10.1364/PRJ.525971>

1. INTRODUCTION

The field of nanoscale optical thermometry has experienced significant growth recently, becoming crucial in various areas such as materials science [1], biophotonics [2,3], and semiconductor engineering [4]. Among the numerous thermal sensors, such as quantum dots [5,6], fluorescent dyes [7], and nanoparticles [8], quantum defects in solids [9] emerge as particularly noteworthy. Their appeal lies in their robustness, biocompatibility, and wide operating temperature range, maintaining performance even under harsh environmental conditions, e.g., nitrogen-vacancy (NV) centers [10–12] and silicon-vacancy (SiV) centers [9] in nanodiamonds. Most demonstrated thermometry using these defects has relied on techniques such as microwave-involved optically detected magnetic resonance (ODMR) [3] or analyzing the photon properties of zero-phonon lines (ZPLs) [9,13]. However, ODMR methods face challenges due to microwave-induced heating [14] and magnetic field noise sensitivity [15]. Meanwhile, ZPL-based approaches require constant spectral

analysis, limiting their application in terms of speed and temperature resolution.

An emerging all-optical technique that measures the intensity ratio between anti-Stokes and Stokes emissions from color centers [16–19] is gaining prominence for its real-time capabilities, high-temperature sensitivity, and spatial resolution at the diffraction limit. As electronic components continue to miniaturize, efficient thermal management is essential to avert heat accumulation that could compromise device integrity. The integration of this thermometry into semiconductor processes, particularly with CMOS compatibility, heralds new possibilities in computing and electronics, positioning nanoscale optical thermometry as a cornerstone for forthcoming technological and medical breakthroughs [2]. This work demonstrates all-optical thermometry using quantum defects in CMOS-compatible material silicon carbide, circumventing the complexities of dual-laser excitation [17] and spectral analysis [9], simplifying the immediate temperature sensing process. The use of SiC quantum defects not only enhances the

capabilities of nanoscale optical thermometry but also opens up the potential for substantial technological and medical advancements. With SiC's inherent CMOS compatibility feature, this thermometry technique is set for straightforward integration into semiconductor chips, promising widespread industrial applications.

2. METHODS

Color centers are luminescent emitters formed by defects within the solid lattice structure, typically involving missing atoms or substitutions that alter the electronic structure of the atomic-like defect. For instance, the loss of one silicon atom and two adjacent silicon and carbon atoms, respectively, results in the formation of a silicon vacancy [20] and a divacancy [21] in the 4H silicon carbide lattice. When these color centers are excited by above band laser to higher energy levels and release energy in the form of photons when they return to lower levels, resulting in photoluminescence, until now, the most studied color centers in 4H-SiC have been silicon-vacancy and divacancy centers, as depicted in Fig. 1(a). Silicon-vacancy centers [21] are formed by the absence of a silicon atom, which, depending on the silicon atom's position in either the quasi-cubic site k or the hexagonal site h, leads to the formation of V1 and V2 color centers with the ZPLs located at 861 nm and

917 nm [22]. Divacancy centers are composed of adjacent carbon and silicon vacancies. Since carbon and silicon atoms can occupy two inequivalent positions, four types of divacancy configurations are possible: hh, kk, hk, and kh, as shown in Fig. 1(a). The ZPL emission of divacancy centers typically ranges from 1038 nm to 1133 nm [21,23]. Thus, the optimal excitation wavelength of silicon vacancy and divacancy is 780 nm and 920 nm [24]. Such excitation, where the laser photon energy exceeds the fluorescence energy, is known as Stokes excitation [25,26]. Conversely, anti-Stokes excitation occurs when the excitation photon energy is less than that of the energy level. As illustrated in Fig. 1(a), with the help of the phonon, silicon vacancies emit fluorescence at a higher frequency than the absorbed photons under anti-Stokes excitation. In this work, we employ a 980 nm continuous-wave laser (yellow) capable of simultaneously exciting both in 4H-SiC silicon vacancies (anti-Stokes fluorescence) and divacancies (Stokes fluorescence), proposing an experimental scheme for real-time temperature sensing using silicon carbide color centers [27–30]. The energy levels involved in the excitation process for divacancy centers under Stokes excitation (i) and V_{Si} defects under anti-Stokes excitation (ii) are depicted in Fig. 1(a). The yellow arrows indicate optical excitation. For normal Stokes excitation, the energy of the emission photon is less than that of the excitation laser.

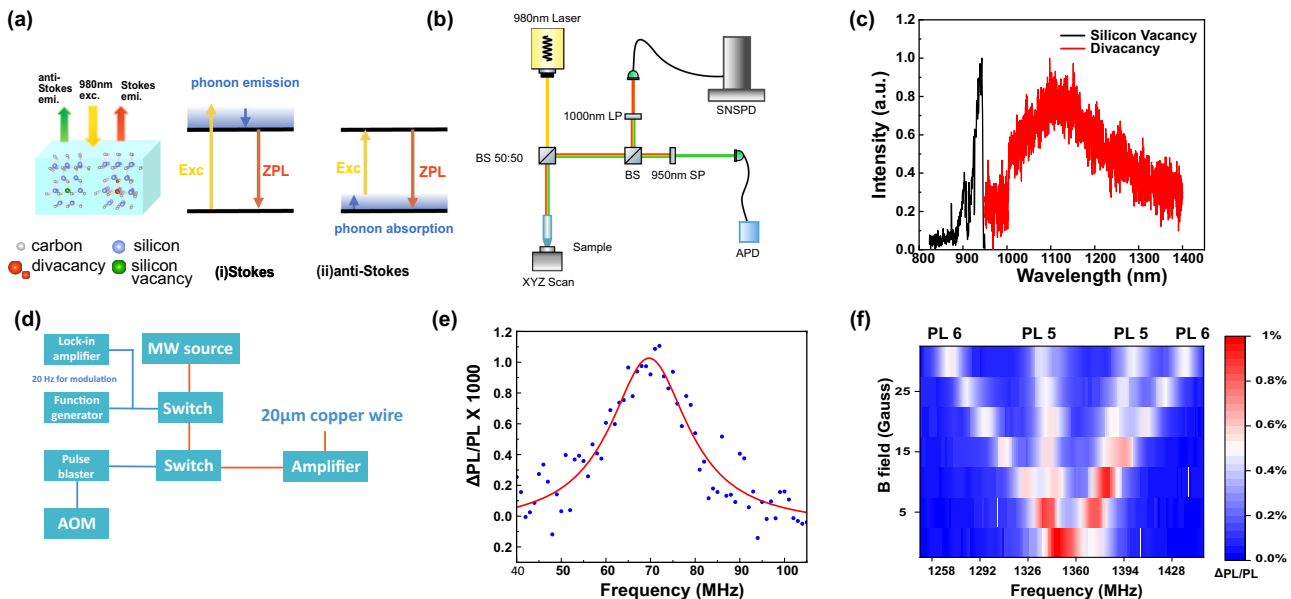


Fig. 1. Characterization of anti-Stokes and Stokes emissions from two types of color centers in 4H-SiC. (a) Excitation and emission schematic: a 980 nm laser is employed to excite silicon vacancies and divacancies simultaneously. The energy level diagram depicts phonon absorption and emission processes during anti-Stokes and Stokes emissions. Energy levels of the excitation process for divacancy centers under Stokes excitation (i) and V_{Si} defects under anti-Stokes excitation (ii). The yellow arrows indicate optical excitation. For normal Stokes excitation, the energy of the emission photon is less than that of the excitation laser, with the phonon sideband emission typically dominating at room temperature. In contrast, for anti-Stokes excitation of silicon-vacancy centers, the photon energy of the laser energy is less than the transition, necessitating phonon absorption, as indicated by the blue square in the energy level diagram. (b) Optical setup schematic: the fluorescence from Si vacancies and divacancies is bifurcated into two channels by a beam splitter and subsequently collected post-filtering by an SNSPD and an APD. Key components are labeled as BS (beam splitter), LP (long-pass filter), and SP (short-pass filter). (c) Photoluminescence spectrum: the emission peaks associated with silicon vacancies (black) and divacancies excited by a 980 nm laser are illustrated. (d) Microwave system diagram: microwaves traverse through a dual-switch setup enabling 20 Hz modulation for continuous waveforms and pulse modulation for rapid spin control. The output feeds into a lock-in amplifier (Stanford Research System SR830) for detection enhancement. (e) ODMR spectrum for silicon-vacancy centers under anti-Stokes excitation. (f) ODMR spectrum for PL5 and PL6 across a magnetic field (0–30 Gauss): the depicted spectra highlight the behavior of PL5 and PL6 emissions under an increasing *c*-axis magnetic field, demonstrating divergent and bending trends, respectively.

the excitation laser, with the phonon sideband emission typically dominating at room temperature. In contrast, for anti-Stokes excitation of silicon-vacancy centers, the photon energy of the laser energy is less than the transition, necessitating phonon absorption, as indicated by the blue square in the energy level diagram. Since the density of phonons is closely related to temperature, an increase in temperature leads to a higher phonon density. This higher phonon density, in turn, promotes anti-Stokes emission. This is the fundamental mechanism underlying our thermometry protocol.

Our sample is an unprocessed chip of 4H-SiC from a stock wafer purchased from Cree Inc. (semi-insulating silicon carbide substrates with serial No. W4TRD0R-0200). The silicon vacancy and divacancy ensembles are present everywhere in the as-purchased material, so the laser excitation spot can be randomly chosen (see Fig. 4). To characterize the two types of intrinsic color centers, we measure the fluorescence using a room-temperature homebuilt confocal microscope system, as shown in Fig. 1(b). Initially, a 980 nm laser is coupled into the confocal microscope system using a single-mode fiber; an objective with a numerical aperture of 0.65 (Olympus, LCPLAN N, 50 \times) focuses the laser on the sample, which is placed on a three-dimensional piezoelectric stage. The power of the excitation laser is 1 mW, which corresponds to a power density of 200 kW/cm². When using an ensemble of color centers in a micrometer-sized crystal where heat cannot dissipate easily such as NV centers in nanodiamonds on a glass, the laser-induced heating resulting from the optical cycles becomes significant and causes a considerable temperature rise within a very short time [3]. However, for bulk SiC material, which has good thermal conductivity (350 W m⁻¹ K⁻¹), this laser heating effect is insignificant due to the minuscule heat influx and the exceptionally high rate of heat dissipation by SiC [31]. The emitted Stokes and anti-Stokes fluorescences are collected through the same objective. The fluorescence is then split into two paths, with Stokes and anti-Stokes fluorescence being filtered using a 1000 nm long-pass filter (Thorlabs, FELH1000) detected with a superconducting nanowire single-photon detector (SNSPD) and a 950 nm short-pass filter detected with a single-photon avalanche diode (APD), respectively. Spectral measurement is a crucial method for characterizing color centers.

3. RESULTS AND DISCUSSION

Figure 1(c) shows the spectra of two types of color centers at room temperature excited by a 980 nm laser. Due to the interaction between electrons and surrounding phonons at room temperature [32], the spectrum exhibits some broadening, i.e., phonon sidebands. The anti-Stokes spectrum of silicon vacancies covers 846 nm to 950 nm, while the Stokes spectrum for divacancies spans 1000 nm to 1400 nm, which is in line with the optical characteristics of silicon vacancies and divacancies. The uneven cutoffs at 950 nm and 1000 nm are due to the filtering effect of the filters on the laser and irrelevant fluorescence. The figure shows that the Stokes fluorescence of divacancies is much stronger than their anti-Stokes fluorescence, aligning with the expectation of lower efficiency for anti-Stokes excitation. To further confirm the defect type,

we perform ODMR of both silicon vacancy and divacancy; we use the setup in Fig. 1(d). The microwave signal initially passes through two switches: the first switch enables 20 Hz modulation, and the second facilitates rapid spin control via pulse modulation. Subsequently, the signal received by the detector is forwarded to a lock-in amplifier (Stanford Research System SR830) for lock-in detection. For the anti-Stokes excitation of silicon vacancy, we got an expected peak at around 70 MHz, as displayed in Fig. 1(e). For the Stokes excitation, since PL5 and PL6 are mixed, we applied a *c*-axis magnetic field from 0 to 30 Gauss. Peaks of PL6 are diverged with a slope of 2.8 MHz per Gauss, while PL5 peaks are bending, the same behavior as in the literature [23,33].

Figure 2(a) depicts a schematic drawing and a photo of our device. We use a single-stage TEC element to heat the sample and control the heating rate uniformly. Thus, we attach the sample to a ceramic piece and apply voltage to the TEC module to transfer heat to the sample, changing its temperature. An attached temperature sensor (platinum resistance temperature detector TH100PT) on the sample helps us monitor its temperature, facilitating the adjustment of the applied voltage. In our experiments, we increased the voltage from 0 V to 16 V, raising the temperature to approximately 500 K. We excited 4H-SiC samples with a 1 mW 980 nm laser (power density of 200 kW/cm²), increasing the temperature from 296 K to 463 K, and measured the changes in fluorescence intensity of silicon-vacancy centers and divacancy centers with temperature, as well as the intensity ratio of anti-Stokes to Stokes fluorescence. Figure 2(b) presents a fitting of the temperature-dependent fluorescence curve under anti-Stokes excitation for silicon-vacancy centers. Each data point was collected over a 20 min period with measurements taken at 50 ms intervals, and the error bars represent the standard deviation of these measurements. We found that the anti-Stokes fluorescence intensity and temperature follow an Arrhenius-type exponential relationship [34–36], fitting the data to $Ae^{\frac{-E_a}{k_B T}}$, where k_B is the Boltzmann constant and $E_a = hc \cdot \left(\frac{1}{\lambda_1} - \frac{1}{\lambda_2} \right)$ is the energy difference between the excitation light and the emitted fluorescence (ZPL) of silicon vacancies. From the fitting, we extracted E_a to be 89.7 meV, which agrees well with the ZPL of silicon-vacancy 917 nm which corresponds to 86.9 meV. The trend indicates an exponential dependence of anti-Stokes fluorescence intensity on temperature, a mechanism highly beneficial for high-sensitivity temperature sensing applications and the fundamental principle of temperature sensing in this work. Figure 2(c) displays the intensity change of Stokes emission with respect to temperature, following an Arrhenius-type relationship, but showing a downward trend. Its physical meaning remains to be further explored. To achieve a practical temperature sensor, we choose the ratios of anti-Stokes to Stokes emission for temperature sensing. Figure 2(d) illustrates the fit for the ratio of anti-Stokes to Stokes fluorescence intensity with temperature changes, fitting the data to an exponential function $a + be^{\frac{c}{T-T_0}}$, with the results showing a high degree of fit. The high dependency of the ratio on temperature translates into exceptionally high sensitivity.

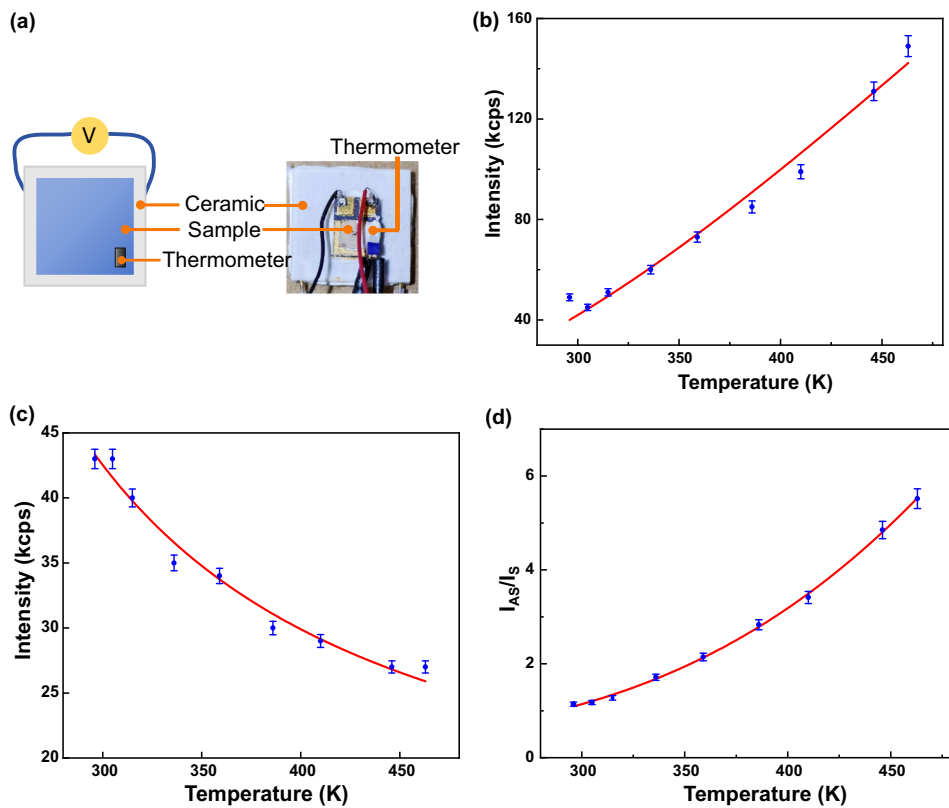


Fig. 2. Characterization of anti-Stokes and Stokes emission. (a) Schematic illustration and a photo of the temperature change device. The sample is attached to a ceramic piece and heated by applying voltage to the TEC module. (b) Temperature dependence of anti-Stokes fluorescence from silicon vacancy. Each data point was collected over a 20 min period with measurements taken at 50 ms intervals, and the error bars represent the standard deviation of these measurements. The data fits well with the Arrhenius-type equation $Ae^{\frac{E_a}{k_B}T}$, and $E_a = 89.7$ meV is coincident with ZPL of silicon-vacancy at 917 nm (86.9 meV). (c) Change of Stokes fluorescence with temperature. (d) Temperature dependence of anti-Stokes to Stokes PL ratio. The ratio fits an exponential curve $a + be^{\frac{f}{T-T_0}}$, showing high sensitivity in temperature sensing applications.

Next, we analyze the stability and sensitivity of this temperature sensing scheme. In all fluorescence-based strategies, the temperature is calculated from the measurement of diverse indicators, such as intensity, intensity ratio, peak position, polarization, and lifetime [2]. The value of these fluorescence indicators can be quantified as Q . The rate of the change of Q associated with temperature T is defined as the absolute sensitivity S_a with $S_a = \frac{dQ}{dT}$. However, due to the different units of measurement, the relative sensitivity S_r is used to compare different systems. This normalizes S_a by the value of the fluorescence indicator, expressed as $S_r = \frac{1}{Q} \frac{dQ}{dT}$. From Fig. 2(d), where Q represents the ratio between anti-Stokes and Stokes emissions, the relative sensitivity at 300 K is $1.06\% \pm 0.02\% \text{ K}^{-1}$. Besides relative sensitivity, temperature resolution η is a typical metric for thermometers. It is the smallest detectable temperature change, determined by the standard deviation δ of the parameter used for temperature determination $\eta = \delta\sqrt{t}$, where t is the integration time. Experimentally, η can be extracted from the shot noise fit. To evaluate the stability of our sensor, we measured the variation of the fluorescence ratio over 20 min, as shown in Fig. 3(a). The data show a fluctuation of 3.1×10^{-3} , indicating relatively stable temperature

detection. Figure 3(b) presents the curve fitting of temperature uncertainty as a function of integration time; from the red line fitting, we extracted the temperature resolution $\eta = 1.19 \text{ K} \cdot \text{Hz}^{-1/2}$ at 1 mW.

Table 1 lists the relative sensitivity and temperature resolution for different color centers and quantum dots based on various observational metrics [5,6,9–12,16,33,37]. The relative sensitivity of our current method is $1.06\% \text{ K}^{-1}$, which is comparable to the best achievable all-optical method using NV centers in nanodiamonds [10]. The temperature resolution $\eta = 1.19 \text{ K} \cdot \text{Hz}^{-1/2}$ has considerable room for improvement. This is because the sample we use is a commercially available wafer without any treatment. Consequently, the density of defects is relatively low, but this parameter could be improved if the silicon vacancy and divacancy are generated through designed ion implantation [38]. Although the microwave-involved ODMR [33] or thermal pulse scheme in SiC or nanodiamonds [12] has superior temperature resolution, it suffers from microwave heat and drift [14]. All-optical spectral shift is an alternative way; however, acquiring spectral itself will increase the sophistication of the setup and limit the acquiring speed [9,10,16], and real-time monitoring with high resolution is tough. Thus, our current

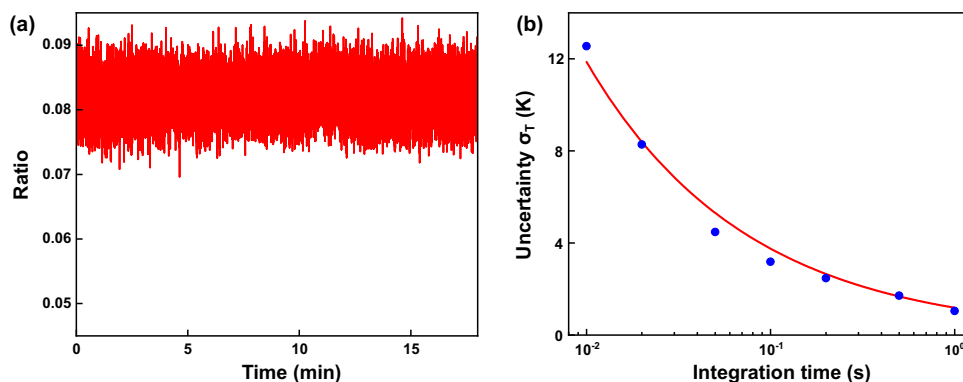


Fig. 3. Attributes of nanoscale thermometry. (a) Longtime trace of anti-Stokes to Stokes PL ratio over 20 min, displaying the stability of measurement. (b) Uncertainty as a function of integration time. The temperature resolution is $\eta_T = \delta_T \sqrt{t_m}$, where t_m is the integration time.

Table 1. Attributes of Different Thermometry Demonstrations Based on NV Centers [10–12], SiV/GeV Centers in Nanodiamonds [9,16]^a

Thermometer	Platform	Methods	Rel Sensitivity (% K ⁻¹)	Temperature Resolution (K · Hz ^{-1/2})	Journal (Year)
V _{Si} /V _{Si} V _C	SiC bulk	All optical (anti-Stokes/Stokes)	1.06	1.19	Our work
V _{Si} V _C	SiC bulk	Microwave [Thermal Carr-Purcell-Meiboom-Gill (TCPMG)]	N.A.	0.0134	<i>Nanoscale</i> (2023) [37]
V _{Si} V _C	SiC bulk	Microwave (ODMR, Ramsey)	N.A.	0.2056	<i>Phys. Rev. Appl.</i> (2017) [33]
GeV/SiV	Nanodiamonds	All optical (anti-Stokes/Stokes)	1.8	0.39	<i>ACS Nano</i> (2023) [16]
NV	Nanodiamonds	Spectral (wavelength shift)	1.0	0.39	<i>Nanotechnology</i> (2015) [10]
SiV	Nanodiamonds	Spectral (wavelength shift)	N.A.	0.512	<i>Appl. Phys. Lett.</i> (2018) [9]
NV	Nanodiamonds	Microwave (ODMR)	N.A.	0.6	<i>Nano Lett.</i> (2021) [11]
NV	Nanodiamonds	Microwave [Thermal Carr-Purcell-Meiboom-Gill (TCPMG)]	N.A.	0.01	<i>Proc. Natl. Acad. Sci.</i> (2013) [12]
Triarylboron	Quantum dots	Spectral (wavelength shift)	0.5	1.0	<i>Angew. Chem. Int. Ed.</i> (2011) [5]
CdTe	Quantum dots	All optical (PL intensity)	2.0	0.8	<i>Small</i> (2012) [6]

^aSilicon-vacancy and divacancy centers in SiC [33,37] and quantum dots [5,6].

technique, which uses a single excitation laser to simultaneously excite both anti-Stokes and Stokes emissions, demonstrates comparable temperature resolution and relative sensitivity to other nanoscale thermometry methods. This technique simplifies the experimental setup, making it a robust and efficient solution for real-time temperature sensing. This is particularly useful given that silicon carbide is becoming one of the most popular materials in various industries and electronics. The sensing technique we demonstrated has the potential to be used in the field of integrated circuits.

4. CONCLUSION

In conclusion, our study advances nanoscale thermometry by demonstrating an all-optical temperature sensing technique using quantum defects in silicon carbide, a material compatible with CMOS processes. This method, leveraging the intensity

ratio between anti-Stokes and Stokes emissions from color centers, offers real-time temperature measurement with high sensitivity and spatial resolution. This method overcomes the traditional defect-based thermometry challenges related to dual-laser excitation and complex spectral analysis. This work not only simplifies temperature sensing at the nanoscale but also paves the way for integrating optical thermometry into semiconductor manufacturing, potentially benefiting temperature monitoring in electronic devices and integrated circuits.

APPENDIX A: ALL-OPTICAL NANOSCALE THERMOMETRY WITH SILICON CARBIDE COLOR CENTERS

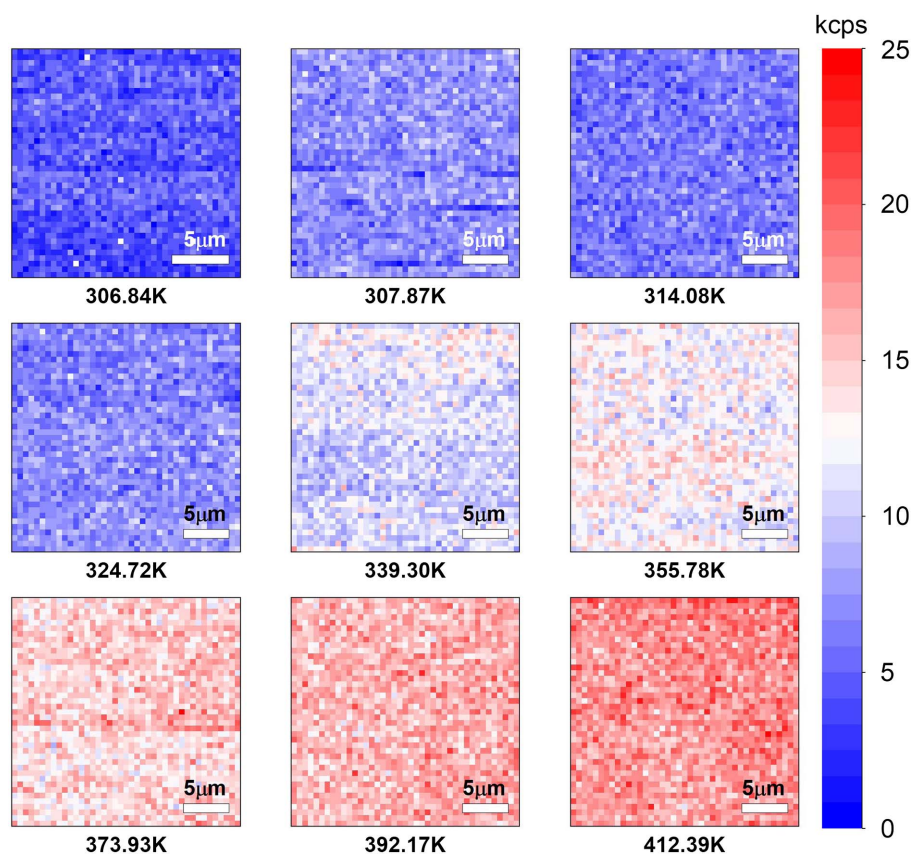


Fig. 4. Confocal scan of Anti-stokes emission at different temperatures from around 306 K to 412 K.

Funding. National Key Research and Development Program of China (2021YFA1400802); National Natural Science Foundation of China (12304568, 12334016, 11934012, 12025402, 62125501, 12261131500, 92250302, 11975221); Guangdong Basic and Applied Basic Research Foundation (2022A1515110382); Guangdong Provincial Quantum Science Strategic Initiative (GDZX2303001, GDZX2306002, GDZX2200001); Shenzhen Fundamental Research Project (JCYJ20230807094408018); Young Elite Scientists Sponsorship Program by CAST; New Cornerstone Science Foundation through the XPLORER PRIZE; Fundamental Research Funds for the Central Universities (2022FRRK030004, 2023FRFK03049).

Disclosures. The authors declare no competing financial interests.

Data Availability. Data underlying the results presented in this paper are not publicly available at this time but may be obtained from the authors upon reasonable request.

REFERENCES

- V. V. Deshpande, S. Hsieh, A. W. Bushmaker, et al., "Spatially resolved temperature measurements of electrically heated carbon nanotubes," *Phys. Rev. Lett.* **102**, 105501 (2009).
- J. Zhou, B. D. Rosal, D. Jaque, et al., "Advances and challenges for fluorescence nanothermometry," *Nat. Methods* **17**, 967–980 (2020).
- G. Kucsko, P. C. Maurer, N. Y. Yao, et al., "Nanometre-scale thermometry in a living cell," *Nature* **500**, 54–58 (2013).
- Y. Li, W. Li, T. Han, et al., "Transforming heat transfer with thermal metamaterials and devices," *Nat. Rev. Mater.* **6**, 488–507 (2021).
- J. Feng, K. Tian, D. Hu, et al., "A triarylboron-based fluorescent thermometer: sensitive over a wide temperature range," *Angew. Chem.* **50**, 8072–8076 (2011).
- P. Haro-González, L. Martínez-Maestro, I. Martín, et al., "High-sensitivity fluorescence lifetime thermal sensing based on CdTe quantum dots," *Small* **8**, 2652 (2012).
- W. Cao, Y. Cui, Y. Yang, et al., "Dyes encapsulated nanoscale metal–organic frameworks for multimode temperature sensing with high spatial resolution," *ACS Mater. Lett.* **3**, 1426–1432 (2021).
- J. Gargiulo, M. Herran, I. L. Violi, et al., "Impact of bimetallic interface design on heat generation in plasmonic Au/Pd nanostructures studied by single-particle thermometry," *Nat. Commun.* **14**, 3813 (2023).
- C. T. Nguyen, R. E. Evans, A. Sipahigil, et al., "All-optical nanoscale thermometry with silicon-vacancy centers in diamond," *Appl. Phys. Lett.* **112**, 203102 (2018).
- T. Plakhotnik, H. Aman, and H.-C. Chang, "All-optical single-nanoparticle ratiometric thermometry with a noise floor of $0.3 \text{ K Hz}^{-1/2}$," *Nanotechnology* **26**, 245501 (2015).
- Y. Wu, M. N. A. Alam, P. Balasubramanian, et al., "Nanodiamond theranostic for light-controlled intracellular heating and nanoscale temperature sensing," *Nano Lett.* **21**, 3780–3788 (2021).
- D. M. Toyli, C. F. de Las Casas, D. J. Christle, et al., "Fluorescence thermometry enhanced by the quantum coherence of single spins in diamond," *Proc. Natl. Acad. Sci. USA* **110**, 8417–8421 (2013).

13. M. Fukami, C. Yale, P. Andrich, *et al.*, "All-optical cryogenic thermometry based on nitrogen-vacancy centers in nanodiamonds," *Phys. Rev. Appl.* **12**, 014042 (2019).
14. Z. Wang, J. Zhang, X. Feng, *et al.*, "Microwave heating effect on diamond samples of nitrogen-vacancy centers," *ACS Omega* **7**, 31538–31543 (2022).
15. M. Fujiwara and Y. Shikano, "Diamond quantum thermometry: from foundations to applications," *Nanotechnology* **32**, 482002 (2021).
16. Y. Chen, C. Li, T. Yang, *et al.*, "Real-time ratiometric optical nanoscale thermometry," *ACS Nano* **17**, 2725–2736 (2023).
17. T. T. Tran, B. Regan, E. A. Ekimov, *et al.*, "Anti-Stokes excitation of solid-state quantum emitters for nanoscale thermometry," *Sci. Adv.* **5**, eaav9180 (2019).
18. J.-F. Wang, F.-F. Yan, Q. Li, *et al.*, "Robust coherent control of solid-state spin qubits using anti-Stokes excitation," *Nat. Commun.* **12**, 3223 (2021).
19. W.-X. Lin, J.-F. Wang, Q. Li, *et al.*, "Room temperature coherent control of a single solid-state spin under anti-Stokes excitation," *Phys. Rev. B* **108**, 235312 (2023).
20. E. Janzén, A. Gali, P. Carlsson, *et al.*, "The silicon vacancy in SiC," *Physica B* **404**, 4354–4358 (2009).
21. W. F. Koehl, B. B. Buckley, F. J. Heremans, *et al.*, "Room temperature coherent control of defect spin qubits in silicon carbide," *Nature* **479**, 84–87 (2011).
22. F. Fuchs, B. Stender, M. Trupke, *et al.*, "Engineering near-infrared single-photon emitters with optically active spins in ultrapure silicon carbide," *Nat. Commun.* **6**, 7578 (2015).
23. A. L. Falk, B. B. Buckley, G. Calusine, *et al.*, "Polytype control of spin qubits in silicon carbide," *Nat. Commun.* **4**, 1819 (2013).
24. G. Wolfowicz, C. P. Anderson, A. L. Yeats, *et al.*, "Optical charge state control of spin defects in 4H-SiC," *Nat. Commun.* **8**, 1876 (2017).
25. A. Cantarero, "Raman scattering applied to materials science," *Procedia Mater. Sci.* **9**, 113–122 (2015).
26. C. H. Camp, Jr. and M. T. Cicerone, "Chemically sensitive bioimaging with coherent Raman scattering," *Nat. Photonics* **9**, 295–305 (2015).
27. C.-F. Liu, W.-H. Leong, K. Xia, *et al.*, "Ultra-sensitive hybrid diamond nanothermometer," *Natl. Sci. Rev.* **8**, nwaa194 (2021).
28. F. Haupt, A. Imamoglu, and M. Kroner, "Single quantum dot as an optical thermometer for millikelvin temperatures," *Phys. Rev. Appl.* **2**, 024001 (2014).
29. P. Neumann, I. Jakobi, F. Dolde, *et al.*, "High-precision nanoscale temperature sensing using single defects in diamond," *Nano Lett.* **13**, 2738–2742 (2013).
30. J.-W. Fan, I. Cojocaru, J. Becker, *et al.*, "Germanium-vacancy color center in diamond as a temperature sensor," *ACS Photonics* **5**, 765–770 (2018).
31. J. L. Braun, C. J. Szwejkowski, A. Giri, *et al.*, "On the steady-state temperature rise during laser heating of multilayer thin films in optical pump–probe techniques," *J. Heat Transfer* **140**, 052801 (2018).
32. L. Besombes, K. Kheng, L. Marsal, *et al.*, "Acoustic phonon broadening mechanism in single quantum dot emission," *Phys. Rev. B* **63**, 155307 (2001).
33. Y. Zhou, J. Wang, X. Zhang, *et al.*, "Self-protected thermometry with infrared photons and defect spins in silicon carbide," *Phys. Rev. Appl.* **8**, 044015 (2017).
34. F. Jensen, "Activation energies and the Arrhenius equation," *Qual. Reliab. Eng. Int.* **1**, 13–17 (1985).
35. R. B. Haj-Kacem, N. Ouerfelli, J. Herráez, *et al.*, "Contribution to modeling the viscosity Arrhenius type-equation for some solvents by statistical correlation analysis," *Fluid Phase Equilib.* **383**, 11–20 (2014).
36. R. B. Nuernberg, "Numerical comparison of usual Arrhenius-type equations for modeling ionic transport in solids," *Ionics* **26**, 2405–2412 (2020).
37. Q.-Y. Luo, S. Zhao, Q.-C. Hu, *et al.*, "High-sensitivity silicon carbide divacancy-based temperature sensing," *Nanoscale* **15**, 8432–8436 (2023).
38. J.-F. Wang, Q. Li, F.-F. Yan, *et al.*, "On-demand generation of single silicon vacancy defects in silicon carbide," *ACS Photonics* **6**, 1736–1743 (2019).